

# Scintillating crystals for the Neutral Particle Spectrometer in JLab Hall C

T. Horn,<sup>1,2</sup> V.V. Berdnikov,<sup>1</sup> S. Ali,<sup>1</sup> A. Asaturyan,<sup>3</sup> M. Carmignotto,<sup>2</sup> J. Crafft,<sup>2</sup> A. Demarque,<sup>4</sup> R. Ent,<sup>2</sup> G. Hull,<sup>5</sup> H-S. Ko,<sup>5,6</sup> M. Mostafavi,<sup>4</sup> C. Munoz-Camacho,<sup>5</sup> A. Mkrtchyan,<sup>3</sup> H. Mkrtchyan,<sup>3</sup> T. Nguyen Trung,<sup>5</sup> I.L. Pegg,<sup>1</sup> E. Rindel,<sup>5</sup> A. Somov,<sup>2</sup> V. Tadevosyan,<sup>3</sup> R. Trotta,<sup>1</sup> S. Zhamkochyan,<sup>3</sup> R. Wang,<sup>5</sup> and S. A. Wood<sup>2</sup>

<sup>1</sup>*The Catholic University of America, Washington, DC 20064*

<sup>2</sup>*Thomas Jefferson National Accelerator Facility, Newport News, Virginia 23606, USA*

<sup>3</sup>*A. I. Alikhanyan National Science Laboratory, Yerevan 0036, Armenia*

<sup>4</sup>*Laboratoire de Chimie Physique, CNRS/Université Paris-Sud, Bât. 349, 91405 Orsay, France*

<sup>5</sup>*Institut de physique nucléaire d'Orsay, 15 rue Georges Clemenceau, 91406 Orsay, France*

<sup>6</sup>*Seoul National University, 1 Gwanak-ro, Gwanak-gu, 08826 Seoul, Korea*

(Dated: September 10, 2019)

This paper discusses the quality and performance of currently available PbWO<sub>4</sub> crystals of relevance to high-resolution electromagnetic calorimetry, e.g. detectors for the Neutral Particle Spectrometer at Jefferson Lab or those planned for the Electron-Ion Collider. Since the construction of CMS and early PANDA ECAL the worldwide availability of high quality PbWO<sub>4</sub> production has changed dramatically. We report on our studies of crystal samples from SICCAS/China and CRYTUR/Czech Republic that were produced between 2014 and 2019.

Keywords: Electromagnetic calorimeters, scintillator, crystal, glass, photo-luminescence, radiation damage, Electron-Ion Collider

## I. INTRODUCTION

Gaining a quantitative description of the nature of strongly bound systems is of great importance for our understanding of the fundamental structure and origin of matter. Nowadays, the CEBAF at Jefferson Lab has become the world's most advanced particle accelerator for investigating the nucleus of the atom, the protons and neutrons making up the nucleus, and the quarks and gluons inside them. The 12-GeV beam will soon allow revolutionary access to a new representation of the protons inner structure. In the past, our knowledge has been limited to one-dimensional spatial densities (form factors) and longitudinal momentum densities (parton distributions). This cannot describe the protons true inner structure, as it will, for instance, be impossible to describe orbital angular momentum an important aspect for nucleon spin for which we need to be able to describe the correlation between the momentum and spatial coordinates. A three-dimensional description of the nucleon has been developed through the Generalized Parton Distributions (GPDs) and the Transverse Momentum-Dependent parton distributions (TMDs). GPDs can be viewed as spatial densities at different values of the longitudinal momentum of the quark, and due to the space-momentum correlation information encoded in the GPDs, can link through the Ji sum rule to a partons angular momentum. The TMDs are functions of both the longitudinal and transverse momentum of partons, and they offer a momentum tomography of the nucleon complementary to the spatial tomography of GPDs.

The two-arm combination of neutral-particle detection and a high-resolution magnetic spectrometer offers unique scientific capabilities to push the energy scale for studies of the transverse spatial and momentum struc-

ture of the nucleon through reactions with neutral particles requiring precision and high luminosity. It enables precision measurements of the deeply-virtual Compton scattering cross section at different beam energies to extract the real part of the Compton form factor without any assumptions. It allows measurements to push the energy scale of real Compton scattering, the process of choice to explore factorization in a whole class of wide-angle processes, and its extension to neutral pion photo-production. It further makes possible measurements of the basic semi-inclusive neutral-pion cross section in a kinematical region where the QCD factorization scheme is expected to hold, which is crucial to validate the foundation of this cornerstone of 3D transverse momentum imaging.

The Neutral-Particle Spectrometer in Hall C will allow accurate access to measurements of hard exclusive (the recoiling proton stays intact in the energetic electron-quark scattering process) and semi-inclusive (the energy loss of the electron-quark scattering process gets predominantly absorbed by a single pion or kaon) scattering processes. To extract the rich information on proton structure encoded in the GPD and TMD frameworks, it is of prime importance to show in accurate measurements, pushing the energy scales, that the scattering process is understood. Precision measurements of real photons or neutral-pions with the NPS offer unique advantages here.

The NPS science program currently features four fully approved experiments [1–4]. E12-13-007 [1] will measure basic cross sections of the semi-inclusive  $\pi^0$  electro-production process off a proton target, at small transverse momentum (scale  $P_{h\perp} \approx \Lambda$ ). These neutral-pion measurements will provide crucial input towards our validation of the basic SIDIS framework and data analysis at JLab energies, explicitly in terms of validation of an-

72 ticipated (x, z) factorization. E12-13-010 will perform  
 73 high precision measurements of the Exclusive Deeply  
 74 Virtual Compton Scattering (DVCS) and  $\pi^0$  cross sec-  
 75 tion [2]. The azimuthal, energy and helicity dependences  
 76 of the cross section will all be exploited in order to sepa-  
 77 rate the DVCS-BH interference and DVCS contributions  
 78 to each of the Fourier moments of the cross section [5].  
 79 The goal of E12-14-003 [3] to measure the cross-section  
 80 for Real Compton Scattering (RCS) from the proton  
 81 in Hall C at incident photon energies of 8 GeV ( $s =$   
 82  $15.9 \text{ GeV}^2$ ) and 10 GeV ( $s = 19.6 \text{ GeV}^2$ ) over a broad  
 83 span of scattering angles in the wide-angle regime. The  
 84 precise cross-section measurements at the highest possi-  
 85 ble photon energies over a broad kinematic range will  
 86 be essential in order to confirm whether the factoriza-  
 87 tion regime has been attained and investigate the nature  
 88 of the factorized reaction mechanism. The differential  
 89 cross section of the  $\gamma p \rightarrow \pi^0 p$  process in the range of  
 90  $10 \text{ GeV}^2 < s < 20 \text{ GeV}^2$  at large pion center-of-mass  
 91 angles of  $55^\circ < \theta_{cm} < 105^\circ$  will be measured in ex-  
 92 periment E12-14-005 [4]. Hard exclusive reactions pro-  
 93 vide an excellent opportunity to study the complicated  
 94 hadronic dynamics of underlying subprocesses at par-  
 95 tonic level. The exclusive photoproduction of mesons  
 96 with large values of energy and momentum transfers  
 97 ( $s \sim t \sim u \gg \Lambda$ ) are among the most elementary  
 98 reactions due to minimal total number of constituent  
 99 partons involved in these  $2 \rightarrow 2$  reactions.

100 The NPS consists of an electromagnetic calorimeter  
 101 preceded by a sweeping magnet. As operated in Hall  
 102 C, it replaces one of the focusing spectrometers. To  
 103 address the experimental requirements the NPS has the  
 104 following components:

- 105 • A 25 msr neutral particle detector consisting of  
 106 1080 PbWO4 crystals in a temperature-controlled  
 107 frame including gain monitoring and curing sys-  
 108 tems
- 109 • HV distribution bases with built-in amplifiers for  
 110 operation in a high-rate environment
- 111 • Essentially deadtime-less digitizing electronics to  
 112 independently sample the entire pulse form for  
 113 each crystal
- 114 • A vertical-bend sweeping magnet with integrated  
 115 field strength of 0.3 Tm to suppress and eliminate  
 116 charged background.
- 117 • Cantelevered platforms off the Super-High Mo-  
 118 mentum Spectrometer (SHMS) carriage to allow  
 119 for remote rotation (in the small angle range), and  
 120 platforms to be on the SHMS carriage (in the large  
 121 angle range)
- 122 • A beam pipe with as large critical angle as possible  
 123 to reduce beamline-associated backgrounds

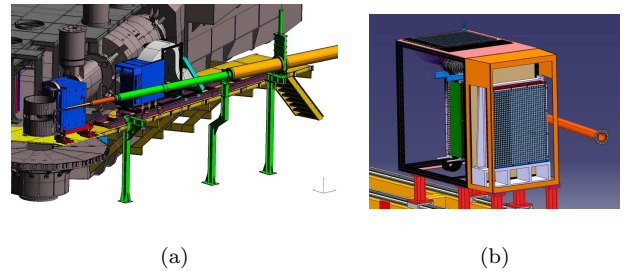


FIG. 1: (Color online) Right: drawing of the NPS spectrometer in Hall C (right). The cylinder on lower left is the target, behind it in the pivot area is the NPS magnet, followed by the NPS calorimeter sitting on a rail system to allow for movement towards/away from the pivot. The dark gray structure is the SHMS; left: NPS calorimeter drawing with details of the crystal matrix inside the frame.

High-Momentum Spectrometer (HMS) for high-precision absolute cross section measurements. In coincidence, systematic point-to-point uncertainties of well below 2% are foreseen with this setup.

Good optical quality and radiation hard PbWO<sub>4</sub> crystals are essential for the NPS calorimeter. Such crystals or more cost-effective alternatives are also of great interest for the Hall D Forward Calorimeter and the high-resolution inner calorimeters at the Electron-Ion Collider (EIC), a new experimental facility that will provide a versatile range of kinematics, beam polarizations and beam species, which is essential to precisely image the sea quarks and gluons in nucleons in nuclei and to explore the new QCD frontier of strong color fields in nuclei and to resolve outstanding questions in understanding nucleons and nuclei on the basis of QCD. One of the main goals of the EIC is the three-dimensional imaging of nucleon and nuclei and unveiling the role of orbital angular motion of sea quarks and gluons in forming the nucleon spin. Details about the EIC science, detector requirements, and design considerations can be found in the EIC White Paper [6] and Detector Handbooks [7].

The common requirements of these electromagnetic calorimeters on the active scintillating material are: 1) good resolution in angle to at least 1 degree to distinguish between clusters, 2) energy resolution to a few  $\%/\sqrt{E}$  for measurements of the cluster energy, and 3) the ability to withstand radiation down to at least 1 degree with respect to the beam line. In this article we discuss the ongoing effort to understand the performance and selection of full-sized scintillator blocks for the NPS, as well as possible alternatives to crystals.

This article is organized as follows: section II describes the basic principle of neutral particle detection, specific NPS requirements, and specifications on the scintillator material, section III reviews the scintillator fabrication, section IV describes experimental methods used in the investigation of the scintillator sam-

162 ples. The results of the measurements of scintillator  
 163 properties, such as optical transmittance, emission spec-  
 164 tra, decay times, light yield, and light yield uniformity  
 165 are discussed in section V. Section VI discusses the re-  
 166 sults on radiation damage and possible curing strate-  
 167 gies. Scintillator structure and impurity analysis are  
 168 presented in section VII. Section VIII discusses the de-  
 169 sign, construction, and commissioning of a single counter  
 170 to test the scintillator performance, section IX contains  
 171 an overview of alternative scintillator material, and sec-  
 172 tiob X presents the summary and conclusions.

## 173 II. EXPERIMENTAL REQUIREMENTS ON 174 NEUTRAL PARTICLE DETECTION

175 Electromagnetic calorimeters are designed to measure  
 176 the energy of a particle as it passes through the detector  
 177 by stopping or absorbing most of the particles coming  
 178 from a collision. The summed deposited energy is pro-  
 179 portional and a good measure of the incident energy. An  
 180 important requirements is thus the linearity of the scin-  
 181 tillator material light response with the incident photon  
 182 energy, i.e. the energy resolution. The segmentation of  
 183 the calorimeter provides additional information and al-  
 184 lows for discriminating single photons from, e.g., DVCS  
 185 and two photons from  $\pi^0$  decay, and electrons from pi-  
 186 ons.

187 The NPS science program requires neutral particle de-  
 188 tection over an angular range between 6 and 57.3 degrees  
 189 at distances of between 3 meter and 11 meter <sup>1</sup> from the  
 190 experimental target, and with 2-3 mm spatial and 1-2%  
 191 energy resolution. Electron beam energies of 6.6, 8.8,  
 192 and 11 GeV will be used. The individual NPS experi-  
 193 ment requirements are listed in Table I.

194 The photon detection is the limiting factor of the ex-  
 195 periments. Exclusivity of the reaction is ensured by the  
 196 missing mass technique and the missing-mass resolution  
 197 is dominated by the energy resolution of the calorimeter.  
 198 The scintillator material should thus have properties to  
 199 allow for an energy resolution of  $1 - 2\%/\sqrt{(E)}$ .

200 The expected rates of the NPS experiments in the  
 201 high luminosity Hall C range up to 1 MHz per module.  
 202 The scintillator material response should thus be fast,  
 203 and respond on the tens of nanosecond level.

204 Given the high luminosity and very forward angles  
 205 required in the experiments, radiation hardness is also  
 206 an essential factor when choosing the detector mate-  
 207 rial. The anticipated doses depend on the experimen-  
 208 tal kinematics and are highest at the small forward an-  
 209 gles. Based on background simulations dose rates of 1-5  
 210 kRad/hour are anticipated at the most forward angles.  
 211 The integrated doses for E12-13-010 are 1.7 MRad at  
 212 the center and 3.4 MRad at the edges of the calorime-  
 213 ter. The integrated doses for the other experiments are  
 214  $< 500$  kRad. The ideal scintillator material would be  
 215 radiation hard up to these doses. The ideal material  
 216 would also be independent of environmental factors like

217 temperature.

### 218 A. Choice of scintillator material

219 The material of choice for the NPS calorimeter is rect-  
 220 angular PbWO<sub>4</sub> crystals of 2.05 by 2.05 cm<sup>2</sup> (each 20.0  
 221 cm long). The crystals are arranged in a 30 x 36 matrix,  
 222 where the outer layers only have to catch the showers.  
 223 This amounts to a total of 1080 PbWO<sub>4</sub> crystals. Each  
 224 crystal covers 5 mrad, and the expected angular res-  
 225 olution is 0.5-0.75 mrad, which is comparable with the  
 226 resolution of the High Momentum Spectrometer (HMS),  
 227 one of the well established Hall C spectrometers. The  
 228 energy resolution of PbWO<sub>4</sub> was parameterized for the  
 229 Primex experiment in Ref. [8]. There, a matrix of 1152  
 230 PbWO<sub>4</sub> crystals was used with incident photons ener-  
 231 gies of 4.9-5.5 GeV. The resulting parameterization is  
 232  $\sigma/E=0.009+0.025/\sqrt{E}+0.010/E$ , where  $E$  is the inci-  
 233 dent beam energy. A  $\pi^0$  missing mass resolution of  $\sim 1$ -2  
 234 MeV and production angle resolution of  $\sim 3$ mrad were  
 235 obtained. and is consistent with NPS experiment re-  
 236 quirements.

237 The emission of PbWO<sub>4</sub> includes up to three com-  
 238 ponents, and increases with increasing wave length [9]:  
 239  $\tau_1 \sim 5$  ns (73%);  $\tau_2 \sim 14$  ns (23%) for emission of  $\lambda$   
 240 in the range of 400-550 nm;  $\tau_3$  has a lifetime more than  
 241 100 ns, but it is only  $\sim 4\%$  of the total intensity. The  
 242 time resolution of the calorimeter based on PbWO<sub>4</sub> is  
 243 thus sufficient to handle rates up to  $\sim 1$  MHz per block.

244 PbWO<sub>4</sub> crystals suffer radiation damage [11–14], but  
 245 optical properties can be recovered [10]. Studies at LHC  
 246 suggest that the conservative dose limit for curing is 50  
 247 to a few 100 krad [15, 16]. If energy resolution is not a  
 248 big issue, the limiting dose may be increased to a few  
 249 MRad. The NPS includes a light monitoring and curing  
 250 system to recover the crytal optical properties. These  
 251 systems were tested with a prototye as discussed in sec-  
 252 tion VI. The scintillation light output, decay time, and  
 253 radiation resistance of PbWO<sub>4</sub> are temperature depen-  
 254 dent [17–19], with the light yield increasing at low tem-  
 255 perature, but decay time and radiation resistance de-  
 256 creasing with temperatures. The NPS design will thus  
 257 be thermally isolated and be kept at constant tempera-  
 258 ture to within 0.1°C to guarantee 0.5% energy stability  
 259 for absolute calibration and resolution.

### 260 B. Specifications on Scintillator Material

261 The experimental requirements shown in Table I can  
 262 be translated into specifications on the scintillator mate-  
 263 rial, e.g. PbWO<sub>4</sub> crystals. Besides specifications related  
 264 to dimension and optical properties, minimum limits on  
 265 radiation hardness are also defined for scintillator ma-  
 266 terial fabricated for operation in a high radiation envi-  
 267 ronment like for the NPS or the EIC. Table II lists the

<sup>1</sup> the minimum NPS angle at 3m is 8.5 degrees, at 4m it is 6 degrees

TABLE I: NPS experiment requirements. Electron beam energies of 6.6, 8.8, and 11 GeV will be used.

Parameter	E12-13-010	E12-14-007	E12-14-003	E12-13-005
Photon angl. res. (mrad)	0.5-0.75	0.5-0.75	1-2	1-2
Energy res. (%)	$(1-2)/\sqrt{E}$	$(1-2)/\sqrt{E}$	$5/\sqrt{E}$	$5/\sqrt{E}$
Photon energies (GeV)	2.7-7.6	0.5-5.7	1.1-3.4	1.1-3.4
Luminosity ( $\text{cm}^{-2}\text{sec}^{-1}$ )	$\sim 10^{38}$	$\sim 10^{38}$	$\sim 10^{38}$	$\sim 10^{38}$
Acceptance (msr)	60%/25 msr		60%/25 msr	10-60%/25 msr
Beam current ( $\mu\text{A}$ )	5-50	5-50	5-60, +6% Cu	5-60, +6% Cu
Targets	10cm LH2	10 cm LH2	10 cm LH2	10 cm LH2

268 physical goals and specifications for NPS in comparison  
269 to those for EIC and other projects.

### 270 III. GROWTH AND PRODUCTION OF 271 CRYSTALS

272 The quality of scintillator material, e.g. crystals, de-  
273 pends strongly on the production process and associated  
274 quality assurance. In this section we review the benef-  
275 its and limitations of production methods for  $\text{PbWO}_4$   
276 crystal growth and their implementation at the only two  
277 vendors with mass production capability of such mate-  
278 rials worldwide.

#### 279 A. Crystal growth methods

280 Crystal growth can roughly classified into three  
281 groups: solid-solid, liquid-solid and gas-solid processes,  
282 depending on which phase transition is involved in the  
283 crystal formation. The liquid-solid process is one of the  
284 oldest and widely used techniques. Crystal growth from  
285 melt is the most popular method.

286 The Bridgman technique is one of the oldest method  
287 used for growing crystals. The principle of the Bridg-  
288 man technique is the directional solidification by trans-  
289 lating a melt from the hot zone to the cold zone of the  
290 furnace. At first the polycrystalline material in the cru-  
291 cible needs to be melted completely in the hot zone and  
292 be brought into contact with a seed at the bottom of the  
293 crucible. This seed is a piece of single crystal and ensures  
294 a single-crystal growth along a certain crystallographic  
295 orientation.

296 The crucible is then translated slowly into the cooler  
297 section of the furnace. The temperature at the bottom  
298 of the crucible falls below the solidification temperature  
299 and the crystal growth is initiated by the seed at the  
300 melt-seed interface. After the whole crucible is trans-  
301 lated through the cold zone the entire melt converts to  
302 a solid single-crystalline ingot.

303 The Bridgman technique can be implemented in ei-  
304 ther a vertical or a horizontal system configuration. The  
305 concept of these two configurations is similar. The ver-  
306 tical Bridgman technique enables the growth of crystals  
307 in circular shape, unlike the D-shaped ingots grown by  
308 horizontal Bridgman technique. However, the crystals

309 grown horizontally exhibit high crystalline quality and  
310 lower defect densities, since the crystal experiences lower  
311 stress due to the free surface on the top of the melt and  
312 is free to expand during the entire growth process.

313 The Czochralski process is a method of crystal growth  
314 used to obtain single crystals. It take a seed of future  
315 crystal and attach it to the stick, then slowly pulled up  
316 the stick (0.5-13 mm/h) by rotating it in the same time.  
317 The crucible may, or may not, be rotated in the opposite  
318 direction. The seed will grow into much bigger crystal  
319 of roughly cylindrical shape. The seed should be an ori-  
320 ented single crystal. The Czochralski process is more  
321 difficult, and is good for congruently melting materials  
322 (oxides, silicon among others). By precisely controlling  
323 the temperature gradients, rate of pulling and speed of  
324 rotation, it is possible to extract a large, single-crystal  
325 ingot from the melt. This process is normally performed  
326 in an inert atmosphere, such as argon, and in an inert  
327 chamber, such as quartz. Large variety of semiconduc-  
328 tors and crystals, including  $\text{PbWO}_4$  can be grown by  
329 this method.

330 The Czochralski method is one of the major melt-  
331 growth techniques. It is widely used for growing large-  
332 size single crystals for a wide range of commercial and  
333 technological applications. One of the main advantages  
334 of Czochralski method is the relatively high growth rate.

#### 335 B. Brief description of $\text{PbWO}_4$ crystal history

336 Mass production of  $\text{PbWO}_4$  was developed by CMS  
337 in order to produce the crystals required for use at LHC.  
338 During the CMS and early PANDA EMC construction,  
339 two manufacturers, Borogoditsk Technical Chemi-  
340 cal Plant (BTCP) in Russia and The Shanghai Institute  
341 of Ceramics of the Chinese Academy of Sciences (SIC-  
342 CAS) in China, using different crystal growth methods  
343 were available. Essentially all high quality crystals have  
344 been produced at BTCP using the Czochralski growing  
345 method, whereas SICCAS produces crystals using the  
346 Bridgman method. BTCP is now out of business, and  
347 the worldwide availability of high quality  $\text{PbWO}_4$  pro-  
348 duction has changed dramatically.

349 SICCAS produced 1825 crystals out of the about 70k  
350 crystals for the CMS electromagnetic calorimeter (EM-  
351 Cal), 1200 crystals for the JLab Hybrid EmCal, and  
352 a few hundred crystals for the PANDA EMCAL project

TABLE II: PbWO<sub>4</sub> crystal quality specifications for NPS, EIC, HyCAL/FCAL, CMS, and PANDA. The measurements to determine these properties are discussed in the text.

Parameter	Unit	NPS	Hy(F)CAL	EIC	CMS	PANDA
Light Yield (LY) at RT	pe/MeV	≥15	≥9.5	≥15	≥8	≥16
LY (100ms)/LY(1μs)	%	≥90	≥90	≥90	≥90	≥90
Longitudinal Transmission						
at λ=360 nm	%	≥35	≥10	≥35	≥25	≥35
at λ=420 nm	%	≥60	≥55	≥60	≥55	≥60
at λ=620 nm	%	≥70	≥65	≥70	≥65	≥70
Inhomogeneity of Transverse Transmission Δλ at T=50%	nm	≤5	≤6	≤5	≤3	≤3
Induced radiation absorption coefficient <i>dk</i> at λ=420 nm and RT, for integral dose ≥100 Gy	m <sup>-1</sup>	≤1.1	≤1.5	≤1.1	≤1.6	≤1.1
Mean value of <i>dk</i>	m <sup>-1</sup>	≤0.75		≤0.75		≤0.75
Tolerance in Length	μm	≤ ±150	-100/+300	≤ ±150	≤ ±100	≤ ±50
Tolerance in sides	μm	≤ ±50	±0	≤ ±50	≤ ±50	≤ ±50
Surface polished, roughness Ra	μm	≤0.02		≤0.02	≤0.02	
Tolerance in Rectangularity (90°)	degree	≤0.1		≤0.1	≤0.12	≤0.01
Purity specific. (raw material)						
Mo contamination	ppm	≤1		≤1	≤10	≤1
La, Y, Nb, Lu contamination	ppm	≤40		≤40	≤100	≤40

353 between 2011 and 2015. SICCAS has produced ~670  
 354 crystals for the NPS project between 2014 and 2019.  
 355 The characterization of these crystal is described in the  
 356 following sections.

357 The only other producer with mass production capa-  
 358 bility for PbWO<sub>4</sub> in the world is CRYTUR in the Czech  
 359 Republic. CRYTUR started work on PbWO<sub>4</sub> at the  
 360 end of 1995, considerably later than BTCP and SIC-  
 361 CAS, and did not play a major role during the CMS  
 362 EMCal construction. CRYTUR returned its focus on  
 363 PbWO<sub>4</sub> production in the early 2010's through collab-  
 364 orations with PANDA and EIC. CRYTUR is using the  
 365 Czochralski crystal growing method and has been us-  
 366 ing the pre-production crystal materials from BTCP as  
 367 raw material. CRYTUR is expected to produce all ~  
 368 8000 crystals for the PANDA EMCal barrel approxi-  
 369 mately 700 crystals for the NPS. About 350 crystals for  
 370 the NPS project have been delivered between 2018 and  
 371 2019. The characterization of these crystals is described  
 372 in the following sections.

#### 373 IV. CRYSTAL QUALITY ASSURANCE

374 Quality assurance and control of the scintillator ma-  
 375 terial is important for high precision physics measure-  
 376 ments and also an important part of the production pro-  
 377 cess. Measurement of properties important for physics  
 378 can provide feedback for optimizing material formula-  
 379 tion and fabrication process. The acceptable limits for  
 380 the NPS in comparison to those for EIC and other  
 381 projects are listed in Table II.

#### 382 A. Samples

383 A total of 350 PbWO<sub>4</sub> samples from Crytur and 666  
 384 PbWO<sub>4</sub> samples from SICCAS were studied in this in-  
 385 vestigation. The samples had rectangular shape. Their  
 386 nominal dimensions are 2.05 cm x 2.05 cm x 20 cm. The  
 387 longitudinal and transverse dimensions of all samples  
 388 were measured using a Mitutoyo Electric Digital Height  
 389 Gage (~ 1 μm accuracy). Table III lists the average  
 390 dimensions, year of production, crystal grower, and pro-  
 391 duction technology for all samples, and Fig. 2 shows the  
 392 measured dimensions for a subset of XX SICCAS and  
 393 YY Crytur crystals.

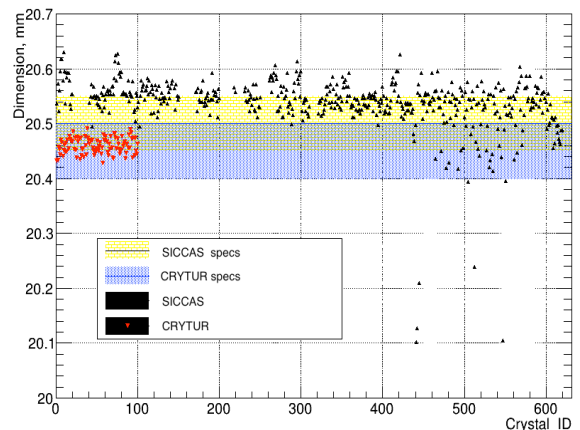


FIG. 2: (Color online) The measured dimensions of the crystals.

394 All crystals from Crytur were grown by the Czochral-

TABLE III: PbWO<sub>4</sub> crystal dimensions.

Vendor	Production Technology	Year of Production	Average dimensions
Crytur	Czochralski	2018	XX
Crytur	Czochralski	2019	XX
SICCAS	Bridgman	2014	200.0 ± 0.2, 20.0 ± 0.02
SICCAS	Bridgman	2015	200.5 ± 0.2, 20.1 ± 0.02
SICCAS	Bridgman	2017/18	XX
SICCAS	Bridgman	2019	XX

395 ski method. Crystals 001 to 100 were produced in 2018,  
 396 crystals 101-350 were produced in 2019. All samples  
 397 from SICCAS were grown using the modified Bridge-  
 398 man method. Crystals 001-015 were produced in 2014,  
 399 crystals 016-045 in 2015, crystals 046-506 in 2017/18,  
 400 and crystals 507 to 666 in 2019. All samples from Cry-  
 401 tur were transparent and clear without major voids and  
 402 scattering centers visible to the eye. A few samples were  
 403 found to be cloudy, which was traced back to the polish-  
 404 ing equipment. One sample had a yellow film, which was  
 405 found to be leftover polishing solution. Samples from  
 406 SICCAS showed yellowish, brownish, and pink color.  
 407 The yellow color may be caused by absorption bands  
 408 in the blue region. Many of the SICCAS samples had  
 409 macroscopic voids and scattering centers visible to the  
 410 eye and highlighted under green laser light. Microscopic  
 411 defects and voids not visible to the eye are discussed in  
 412 section VII A. All surfaces of the samples were polished  
 413 by the manufacturer and no further surface treatment,  
 414 other than simple cleaning with alcohol, was carried out  
 415 before the measurements. Samples were received with-  
 416 out any irradiation exposure. To test the impact of an-  
 417 nealing for new crystals, SICCAS samples 001 to 045  
 418 and 50 samples of 046-506 characterized before and af-  
 419 ter thermal annealing.

## 420 B. Optical transmission

421 The longitudinal transmission was measured using  
 422 a double-beam optical spectrometer with integrating  
 423 sphere (Perkin-Elmer Lambda 950) in the range of wave-  
 424 lengths between 200 and 900 nm. The systematic uncer-  
 425 tainty of transmittance was better than 0.3%. The re-  
 426 producibility of these measurements is better than 0.5%.

427 Additional uncertainties in the transmittance mea-  
 428 surement arise due to the birefringent nature of PbWO<sub>4</sub>  
 429 crystals and due to macroscopic defects, e.g. voids, in-  
 430 clusions, scattering centers. The uncertainty due to bire-  
 431 fringence was estimated to be less than 10% for differ-  
 432 ent azimuthal angle orientations of the crystal. For the  
 433 main measurements the crystal was set up at a specific  
 434 azimuthal angle, which gave the maximum longitudi-  
 435 nal transmittance. The major contribution to uncer-  
 436 tainty in many SICCAS samples was due to macrode-  
 437 fects. The effect was minimized by using an integrating  
 438 sphere, which collected almost all light passing through  
 439 the sample, and collimation of the light path to maxi-

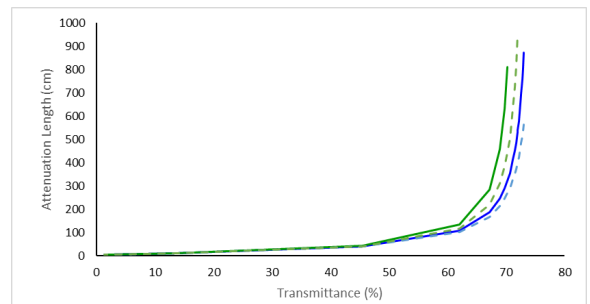


FIG. 3: (Color online) Attenuation length of Crytur crystals at 425nm (solid) and 500nm (dashed) using PbWO<sub>4</sub> ordinary (blue) and extraordinary (green) refractive indices from Ref. [27].

440 mize the longitudinal transmittance.

If one assumes that light impinges normally on the crystal surface and that the two end surfaces are parallel, one can determine the average light attenuation length using [26],

$$L_{attenuation} = \frac{l}{\ln \frac{T(1-T_i)^2}{\sqrt{4T_i^2 + T^2(1-T_i^2)^2 - 2T_i^2}}} \quad (1)$$

where  $l$  is the length of the crystal,  $T$  is the measured transmittance, and  $T_i$  is the real theoretical transmittance limited only at the end surfaces of the crystal. Taking into account multiple reflections,

$$T_i = \frac{1 - R}{1 + R} \quad (2)$$

441 where  $R = (n - n_{air})^2 / (n + n_{air})^2$  with  $n$  and  $n_{air}$  the  
 442 refractive indices of PbWO<sub>4</sub> and air, respectively.

443 The light attenuation length of Crytur and SIC-  
 444 CAS crystals at 425 and 500 nm calculated using  
 445 PbWO<sub>4</sub> ordinary and extraordinary refractive indices  
 446 from Ref. [27] is shown in Fig. 3.

447 The homogeneity of the crystal is investigated based  
 448 on the variation of the transverse optical transmission.  
 449 A quality parameter that characterizes the band edge  
 450 absorption of the crystal is defined as the maximum  
 451 variation of the wavelength at a transmission value of  
 452 T=50% along the length of the crystal. In addition, the  
 453 maximum % deviation of the transverse transmission  
 454 from the value measured at the center are used. Both,  
 455 the transverse optical absorbance and the longitudinal

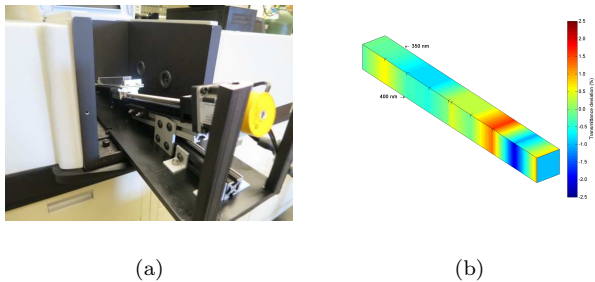


FIG. 4: (Color online) Left: Modification to spectrophotometer for transverse transmittance measurements. Right: 3D transmittance map of a crystal. The low transmittance regions are due to bubbles in the volume.

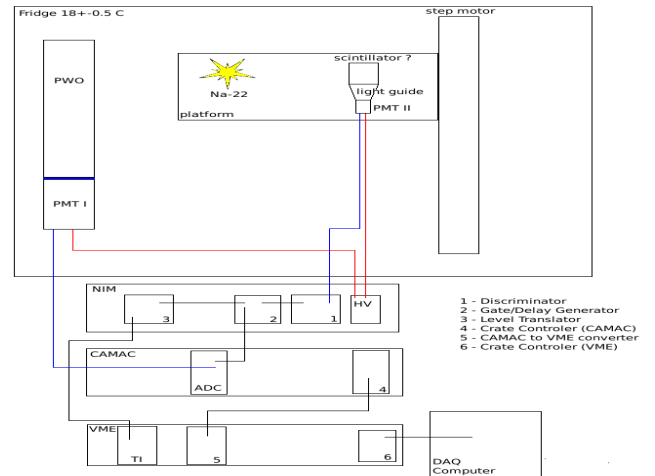


FIG. 5: (Color online) Schematic of the light yield measurement setup inside a temperature-controlled darkbox.

456 transmission were measured as function of wavelength  
457 to characterize the crystal quality.

### 458 C. Luminescence yield, temperature dependence 459 and decay kinetics

460 The scintillation light yield at 18 degrees Celsius was  
461 determined at CUA using a  $^{22}\text{Na}$  source emitting back-  
462 to-back photons of 0.511 keV from  $e^-e^+$  annihilation  
463 (see Fig. 5). One of the end faces of the crystal was opti-  
464 cally coupled to the entrance window of a 2-inch photo-  
465 multiplifier tube (Photonis XP2282, quantum efficiency  
466  $\sim 27\%$  at 400nm) using Bicon BC-630 optical grease.  
467 All other surfaces of the crystal were wrapped in three  
468 layers of Teflon film and two layers of black electrical  
469 tape. The anode signals were directly digitized using a  
470 charge sensitive 11 bit integrating type analog-to-digital  
471 converter (ADC LeCroy 2249W) with integration gates  
472 between 100 ns and 1000 ns, to investigate the contri-  
473 bution of slow components. The effective integration  
474 gate for the main measurements was 150 ns. The photo-  
475 electron number corresponding to the  $\gamma$  source peak  
476 was determined from the peak ADC channel obtained  
477 with a Gaussian fit. To calibrate the signal amplitude  
478 above the pedestal in units of photoelectrons a separate  
479 measurement was made to determine the response to a  
480 single photoelectron.

At fixed gain and fixed light intensity the number of  
detected photoelectrons depends only on the PMT quantum  
efficiency,  $QE \propto N_{pe}$ . Neglecting contributions  
from electronic noise and other possible fluctuations the  
 $N_{pe}$  can be estimated as inverse square of the normalized  
width of the detected photoelectron distribution,

$$N_{pe} = 1/\sigma_{norm}^2, \quad (3)$$

481 where  $\sigma_{norm} = \sigma/N_{ADC}$ , with  $\sigma$  the width of the ampli-  
482 tude distribution determined from a Gaussian fit and  
483  $N_{ADC}$  is the pedestal subtracted signal amplitude in  
484 ADC channels.

485 The setup is operated inside a temperature-controlled  
486 dark box, which provides for temperature accuracy and  
487 stability on the order of better than  $1^\circ\text{C}$ . The depen-  
488 dence of the light yield on the temperature was meas-  
489 ured to be  $2.4\%/^\circ\text{C}$ . This is consistent with previous  
490 measurements published in Ref. [20].

To determine the setup dependence of the light yields,  
subsets of crystals were characterized at IPN-Orsay, as  
well as the facilities at Giessen U. and Caltech. The IPN-  
Orsay facility uses a  $^{137}\text{Cs}$  source. Crystals are wrapped  
in four layers of teflon, 1 layer of aluminum foil, and a  
black heat shrinking tube. The open end is coupled to  
the entrance window of a 2-inch photomultiplier tube  
(Photonis XP5300B) with QE peak around 29%. The  
anode signals were digitized using a Desktop Digitizer  
5730 with effective integration gate 150ns and full range  
up to 1000 ns. At the Giessen facility crystals are excited  
with 662 keV photons from a  $^{137}\text{Cs}$  source. Crystals are  
wrapped in eight layers of teflon, 1 layer of aluminum  
foil, and black heat shrinking tube. The open end is cou-  
pled to a 2-inch PMT (Hamamatsu R2059-01) with typi-  
cal quantum efficiency 20% at 420nm. The PMT signal  
above a suitable threshold were integrated in time gates  
of 100ns to 1000s and digitized with a Charge-to-Digital-  
Converter (CAMAC, Le Croy 2249W). The Caltech fac-  
ility uses the same sources as IPN-Orsay and Giessen.  
The light was detected with a Hamamatsu R2059 PMT  
with quartz window. Crystals were wrapped in one layer  
of Tyvek paper or 5 layers of teflon. Measurements were  
typically made at  $23^\circ\text{C}$ , while measurements at CUA,  
IPN-Orsay, and Giessen are made at  $18^\circ\text{C}$ .

A major difference that affects the absolute number  
of photoelectrons measured with each setup is the quan-  
tum efficiency of the PMTs as discussed in Ref. [21]. The  
gamma-ray excited luminescence of PWO shows a broad  
and complex emission band ranging from 370 to 500 nm.  
The shape of the emission spectrum can be correlated  
with the specific conditions of the crystal synthesis, e.g.

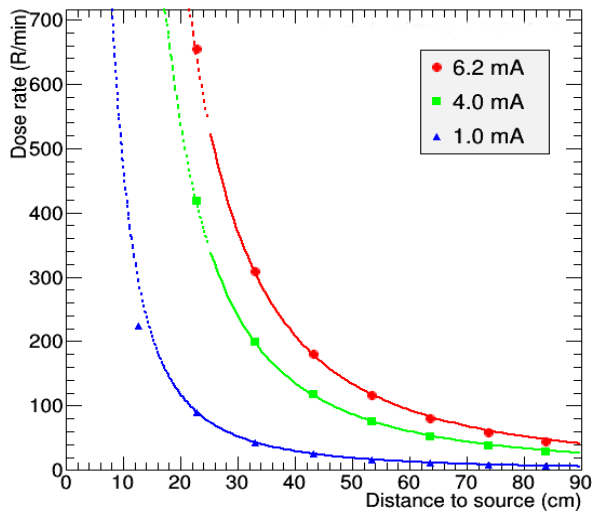


FIG. 6: (Color online) The Faxitron CP160 X-ray dose rate as function of distance from the source.

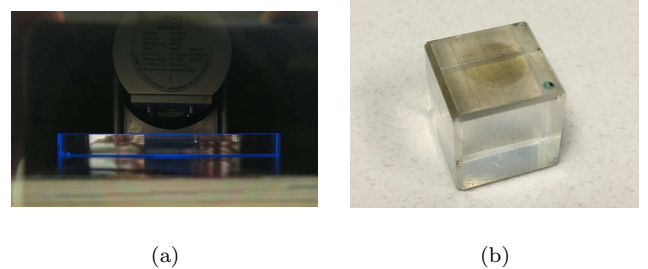


FIG. 7: (Color online) Left: Crystal irradiated by Xrays; Right: Example of radiation damage induced by Xrays and integrated dose of XX Gy.



FIG. 8: (Color online) Irradiation setup with a high activity  $^{60}\text{Co}$  source. Crystals are placed in containers where the radiation dose was previously measured using a Fricke solution.

X-ray photon radiation damage manifests at the surface of the crystal. An example is shown in Fig. 7.

#### D. Gamma ray irradiation

The second irradiation facility was the Laboratoire de Chimie Physique at IPN-Orsay. This facility features a panoramic irradiation complex based on 3000 Ci  $^{60}\text{Co}$  sources. Crystals were irradiated with integrated doses ranging from 500 Gy to 1000 Gy at about 18 Gy/min. The dose rate was accurately measured using Fricke dosimetry, which consists on measuring the absorption of light produced by the increased concentration of ferric ions by ionizing radiation in a solution containing a small concentration of ammonium iron sulfate. The linear absorption with time at a given position determines the exact radiation dose received by the crystal when placed at the same position as the solution.  $\text{PbWO}_4$  crystals were irradiated to 30 Gy at 1 Gy/min.

The  $^{60}\text{Co}$  source allowed for irradiating multiple crystals at the same time. To estimate the dose and dose rate in the crystals, a Fricke solution positioned at the same distance (60 cm from the source) and of the same shape and volume as the crystals was irradiated.

the tungsten concentration in the melt [22]. We thus focus here on the correlations of the measurements between setups rather than absolute values.

The scintillation decay was evaluated by measuring the light yield as a function of the integration gate. This allows for analyzing the relative contribution of slow components. If such slow components contribute significantly an increase in the relative light yield beyond 1000 ns should be clearly visible. In general, the light yield increases by a factor of about three due to cooling to  $-25^\circ\text{C}$  independent of the integration time window.

The gamma ray irradiations were carried out at two different facilities to provide a cross check between measurements. The first was carried out at CUA using the cabinet X-ray (Faxitron CP160). The optical transmittance was determined before and after irradiation with integral doses of 30-100 Gy imposed within an irradiation period of 10 minutes. The crystals were kept light tight during and after irradiation until the transmission measurement commenced to minimize the effect of optical bleaching. The measurement was performed no later than 30 minutes after the end of the irradiation procedure at room temperature. The dose rates (see Fig. 6) were determined using a RaySafe ThinX dosimeter and data provided by the manufacturer. The dose rate at a current of 6.2mA was parameterized as Dose rate (R/min) =  $(-8537 + 55720 \cdot \text{Current}) / \text{Distance}$  to source, where the distance to the source varies between 22.9cm and 83.8cm. The parameterization can be converted to Gy using the conversion factor 0.00877. The dose rate uncertainty was estimated to be XX %. The



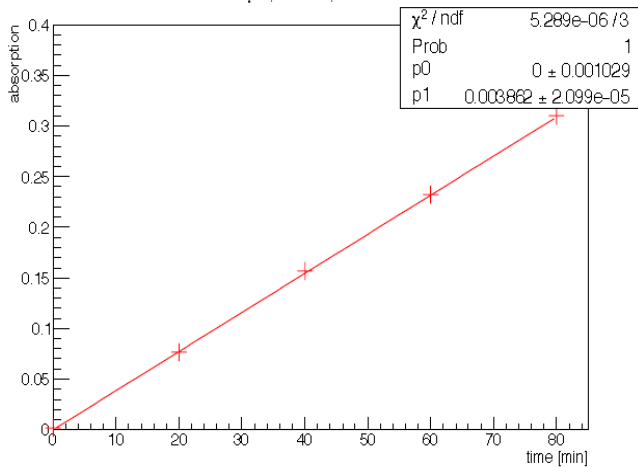


FIG. 9: (Color online) The measured absorbance vs. irradiation time.

Fricke dosimetry is well studied. It changes light absorption linearly under radiation at a given wavelength up to about 200 Gy. The mechanism is the oxidation of ferrous ions ( $\text{Fe}^{2+}$ ) to ferric ions ( $\text{Fe}^{3+}$ ). Ferric ions absorb light and this absorption increases as the dose increases. To quantify the dose rate, we measured the light absorption for different irradiation times at the absorption peak of 304 nm at a distance of 60cm from the source. The result is shown in Fig. 9. The solution's absorbance can be calculated using

$$A = \log \frac{I}{I_0} = \epsilon \times l \times C = \epsilon \times l \times G \times \rho \times D(t)$$

where  $I$  is the measured light intensity through the material,  $\epsilon$  is the molar extinction coefficient ( $2160 + 15$  (T-25) at 304 nm),  $l$  is the optical path,  $C$  is the number of moles transformed by the irradiation,  $G$  is the efficiency for appearance of  $\text{Fe}^{3+}$  ( $1.62 \times 10^{-7}$  mol/J),  $\rho$  is the mass density of the solution, and  $D(t)$  is the radiation dose. The dose rate in Gray per minute is then given by,

$$D(t) = \frac{\Delta A(\text{cm}^{-1})}{\epsilon(\text{Lmol}^{-1}) \times G(\text{molJ}^{-1}) \times \rho(\text{kgL}^{-1})\Delta t(\text{min})}$$

The resulting average dose rate is 1.07 Gy/min with a standard deviation of 0.12 Gy/min.

The impact of radiation effects can be quantified in terms of the change in the absorption coefficient,  $k$ , which is determined from the longitudinal transmittance spectra before and after irradiation using

$$dk = \frac{\ln(T_0/T_{rad})}{d} \quad (4)$$

where  $T_0$  and  $T_{rad}$  are the measured transmittance before and after irradiation and  $d$  is the total crystal length. The change in  $k$  is shown over the entire spectrum of wavelengths in units of  $\text{m}^{-1}$ .

To quantify any setup dependent effects we carried out additional irradiation studies at Caltech and Giessen U. Caltech features a 4000 Ci  $^{60}\text{Co}$  source. Samples were irradiated at 2, 8, 30, 7000 rad/hour. The irradiation facility at the Giessen U Strahlencentrum has a set of five  $^{60}\text{Co}$  sources. The homogeneity of the sources is on the level of 3.6 Gy/min. Samples are irradiated with an integral dose of 30Gy imposed within an irradiation period of 15 minutes. Crystals are kept tight during and after irradiation until transmission is started 30 min after the end of the irradiation.

## E. Electron beam irradiation

The electron beam test was carried out at the Idaho Accelerator Facility, which features a 20 MeV electron beam with 100 Hz repetition rate and peak current  $I_{peak}=111$  mA (11.1 nC per pulse and 100 ns pulse width). The beam is roughly 1 mm in diameter and exits through (1/1000) inch thick Ti window, a  $x/X_0 = 7.1 \times 10^{-4}$  radiation length. Beam position and profile were measured using a glass plate. Scanning the plates and fitting the intensity distribution provides a quantitative (though approximate) measurement of the position and size of the beam at the location of the plate. The front plate was placed at the position of the  $\text{PbWO}_4$  crystal front faces during irradiation that is 10.75 cm from the beam exit window. The rear plate was located at 33 cm from the beam exit, and shows the beam profile expansion. This provides a relatively homogeneous irradiation and heat load on the crystals. The beam profile is shown in Fig. 10.

A  $\text{PbWO}_4$  crystal at the above mentioned beam parameters has received a dose of 216 krad/min. Since such radiation dose rate is much higher ( $\sim 13$  Mrad/h) than the dose rates expected during the actual experiments, our tests were carried out at lower dose rates at a reduced accelerator repetition rate, keeping the beam current per pulse and pulse width unchanged. The measured relative difference of the crystal transmittance before and after irradiation is illustrated in Fig. 20. All transmittance measurements at the Idaho facility were carried out using an OCEAN OPTICS USB4000 device instead of a permanent spectrometer setup. The reproducibility of measurements with this setup ranges from 5% to 15%.

## V. RESULTS CRYSTAL CHARACTERIZATION

### A. Transmittance and light attenuation length

The longitudinal transmittance is shown in Fig. 11. Changes in the transmittance due to irradiation are discussed in section VI.

The transmittance at 800 nm was  $\geq 70\%$  for all Crytur and many SICCAS samples, and thus close to the theo-

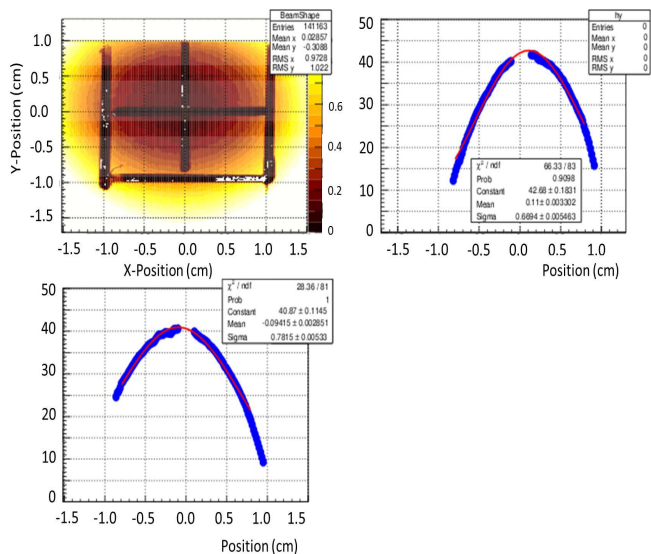
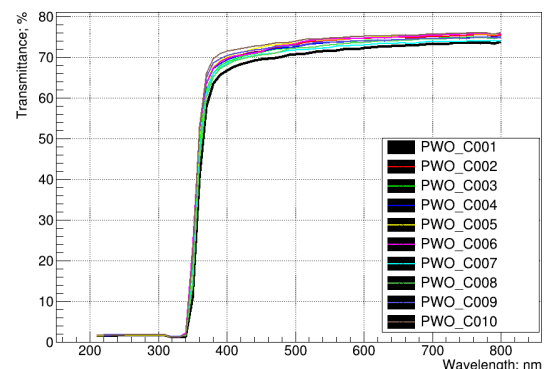
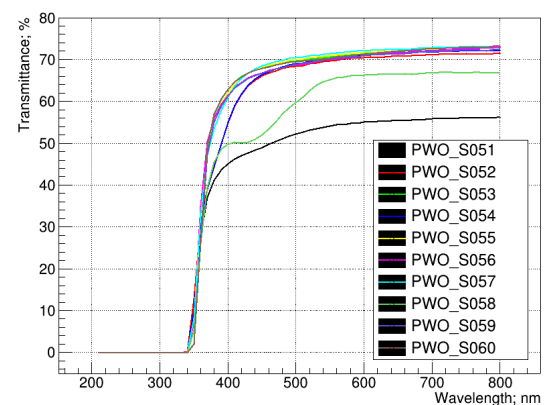


FIG. 10: (Color online) The glass plate exposed at the beginning of test at the Idaho Accelerator Facility (top left). Y (top right) and X (bottom left) profile of the beam at front plate located at 33 cm from the beam exit. Scanning and fitting give  $\sigma_x \sim 0.8$  cm and  $\sigma_y \sim 0.7$  cm).



(a)



(b)

FIG. 11: (Color online) Representative longitudinal transmittance spectra for Crytur crystals produced in 2018-19 (left) and SICCAS crystals produced in 2017 (right).

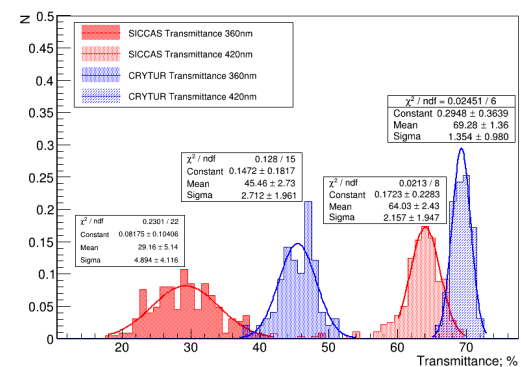


FIG. 12: (Color online) Longitudinal transmittance of Crytur and SICCAS crystals produced 2017-2019.

633 retical limit. This implies a very long light attenuation  
 634 length at this wavelength. No significant absorption was  
 635 observed at wavelengths  $> 550$ nm. For SICCAS samples  
 636 with yellow, pink, or brown color significant absorption  
 637 was observed below 550nm. The origin of the absorption  
 638 is not understood. There are also considerable differ-  
 639 ences in transmittance spectra in the wavelength region  
 640 between 350 and 550nm. Some SICCAS samples have a  
 641 knee below 400nm, others show none. None of the Cry-  
 642 tur samples show a knee. Samples with macro defects  
 643 have very high transmittance at 360nm. The knee in  
 644 the longitudinal transmittance can be correlated with  
 645 radiation resistance. As discussed in section VI, sam-  
 646 ples irradiated with EM radiation and poor resistance  
 647 will exhibit the knee below 400nm as well.

648 Fig. 12 illustrates the uniformity of the longitudinal  
 649 transmittance for XX Crytur and YY SICCAS samples.  
 650 CRYTUR crystals have an average transmittance of  $69.3$   
 651  $\pm 1.4$  % at 420nm and  $45.5 \pm 2.7$  % at 360nm. SICCAS  
 652 crystals have an average transmittance of  $64.0 \pm 2.4$  %  
 653 at 420nm and  $29.2 \pm 5.1$  % at 360nm. The broader  
 654 distributions of the SICCAS crystals can be correlated  
 655 with visual observation of mechanical defects, e.g. sig-  
 656 nificant scattering centers in the bulk, as discussed in  
 657 section IV A.

658 Compared to 23cm long crystals produced by SIC-  
 659 CAS for CMS, the average performance of both Crytur  
 660 and SICCAS crystals produced since 2014 is significantly  
 661 improved. As published in Ref. [23], the average longi-  
 662 tudinal transmittance of CMS crystals is 21.3%, 65.6%,  
 663 and 71.7% at 360nm, 440nm, and 600 nm, respectively.

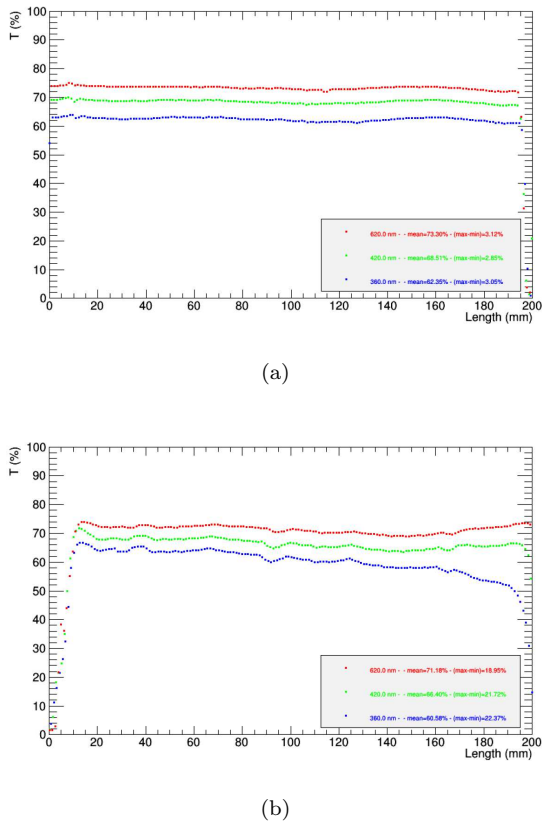


FIG. 13: (Color online) Transmittance transverse along the crystal for a (left) uniform and (right) nonuniform sample.

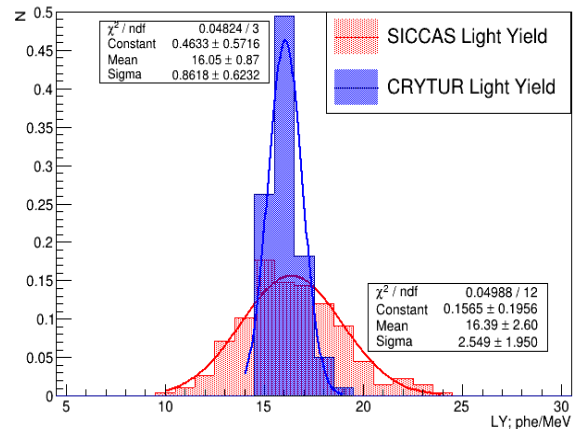


FIG. 14: (Color online) The measured light yield of the crystals.

686 CMS and since 2014 for the NPS project. All measurements were made at room temperature and with a 200ns gate. The average light output of 22x22x230 mm<sup>3</sup> PWO samples from CMS is 10.1 photoelectrons/MeV. In comparison, the 20x20x200 mm<sup>3</sup> PWO samples produced for NPS have an average light yield of 14.1 photoelectrons/MeV.

692 The light yield as a function of integration time was fitted to the parameterization

$$LightOutput = A_0 + A_1 * (1 - e^{-t/\tau}) \quad (5)$$

693 where  $A_0$ ,  $A_1$  and  $\tau$  are fit parameters. The fits show that over the time interval from 0 to 1000ns the decay times can be parameterized with a fast component,  $\tau$  of  $20 \pm 1$  ns.

694 The scintillation decay kinetics is determined as the fraction of the total light output and the light yield integrated in a short time window of 100 ns. The measured values are on average 95% for Crytur and 92% and 99% for SICCAS crystals. The light yields for 50ns and 100ns time windows are very similar and the fractional values are larger than 84% and 96% for CMS PWO crystals[23].

695 The performance of PbWO<sub>4</sub> crystal based calorimeter is highly dependent on the light-collection efficiency from the scintillator to the PMT. We have studied the effect of different reflectors and number of layers of reflectors on the light yield on PWO crystals. Fig. 16 shows the reflectivity of mylar, teflon, and Gore reflectors as measured with a spectrophotometer.

696 Teflon tape is easily available and was our default choice for light yield tests. It is slightly transparent and therefore additional layers increase the reflectivity as shown in Fig. 16. There is a clear positive trend from one to three layers, where the light yield increases as the number of layers increases. The measured light yield follows the same trend as the reflectivity results. Three to four layers of teflon tape is thus the optimum amount.

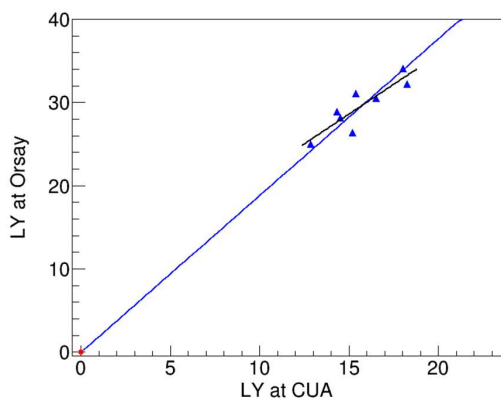
664 The transmittance in the transverse direction (2 cm thickness) was measured at several distances ranging between 5 and 195 mm from the face of the crystal. The results for one SICCAS crystal passing and one not passing specification are shown in Fig. 13.

## 669 B. Light Yield

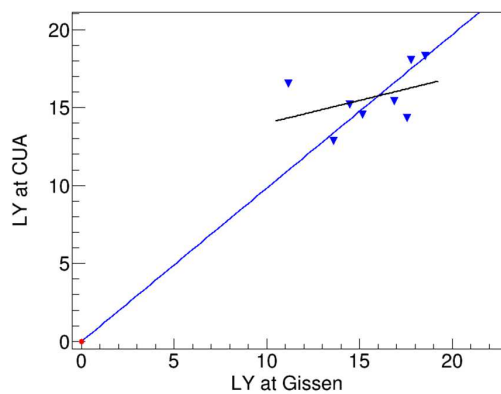
670 The light yield of Crytur and SICCAS samples is shown in Fig. 14. CRYTUR crystals have an average light yield of 16 with a variance of 0.6 photoelectrons/MeV, which is within the uncertainty of the measurement. SICCAS crystals have an average light yield of 17.4 with a variance of 3.8 photoelectrons/MeV. This large variation can be traced back to mechanical and chemical differences in crystals.

671 Measurement correlations between CUA, IPN-Orsay, and Giessen U. are shown in Fig. 15. The light yields of four crystals measured at Caltech and CUA agreed within one photoelectron. The absolute numerical values in photoelectrons to the vendor were given based on photoelectron numbers from the CUA setup.

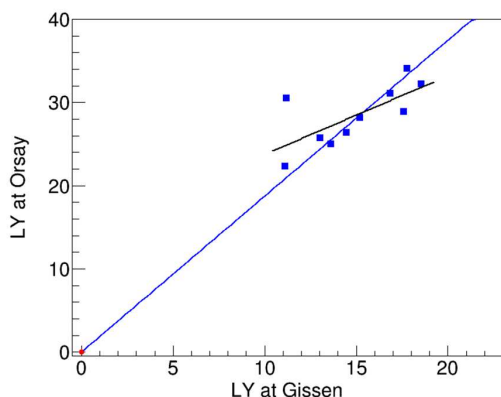
672 Measurements done at Caltech also allowed for a direct comparison of crystals produced by SICCAS for



(a)

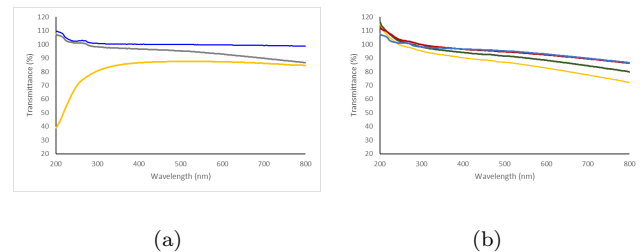


(b)



(c)

FIG. 15: (Color online) Correlations between light yield measurements performed at CUA, IPN-Orsay, and Giessen. See text for details of each setup.



(a)

(b)

FIG. 16: (Color online) Reflectivity of mylar, teflon, and Gore reflectors (left), and teflon of 1, 2, 3, and 5 layers (right).

719 When used as a wrapping material, diffusive reflectors  
 720 like teflon are more effective for light collection at 420  
 721 nm than specular reflectors. For example, mylar Foil  
 722 produced lower light yields than 3 layers of Teflon Tape.  
 723 On the other hand, Enhanced Specular Reflector (ESR)  
 724 produces the same light yield as three layers of teflon.  
 725 The diffusive Gore reflector material has the highest re-  
 726 flectivity at 420 nm and also produced the highest light  
 727 yield compared to both, three layers of teflon and ESR.  
 728 Taking into account the mechanical properties of the  
 729 reflector material and the constraints on total reflector  
 730 thickness imposed by the detector design, the NPS uses  
 731 one layer of  $65\mu\text{m}$  ESR (VM2000). Tests were carried  
 732 out to check for light cross talk between crystals and  
 733 found no significant contamination.

734 It is interesting to note that the location of the re-  
 735 flector on the crystal has different importance for the  
 736 total light collection. This was studied by comparing  
 737 the light yield when the entire crystal was wrapped in  
 738 3 layers of Teflon Tape to those when only the bottom  
 739 half (close to the PMT), the top half, small end face, or  
 740 both end-and-top half were covered with reflector. The  
 741 greatest impact on the light yield came from the reflector  
 742 wrapped around the top half of the crystal resulting  
 743 in a significant reduction of more than 8 photoelectrons  
 744 in light yield when not present.

## 745 VI. RESULTS ON RADIATION DAMAGE

746 Possible effects of radiation damage in a scintillating  
 747 crystal include radiation induced absorption, i.e. color  
 748 center formation, effect on the scintillation mechanism,  
 749 and radiation induced phosphorescence. Color center  
 750 formation would affect the light attenuation length, and  
 751 so the light output measured with the photodetector.  
 752 Damage to the scintillation mechanism could affect the  
 753 light output. Radiation induced phosphorescence could  
 754 cause additional noise in the readout instrumentation.

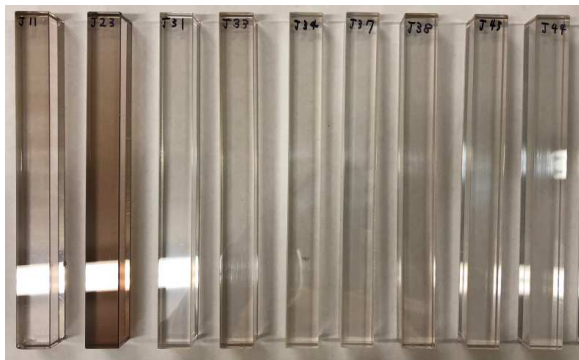


FIG. 17: (Color online) Visual inspection of crystals after 30 Gy of radiation at 1 Gy/min

### A. Light Attenuation

Figure 17 illustrates the impact of an integral dose of 30 Gy at a dose rate of 1 Gy/min on a subset of 10 SICCAS samples. The radiation resistance varies considerably from sample to sample. While color center formation is significant in J23 giving the sample a brown color, J31 appear completely unaffected.

The impact on transmittance can be seen in Fig. 18. A sample of good radiation resistance has small variation in transmittance before and after irradiation. On the other hand, one observes significant radiation induced absorption throughout the spectrum, and in particular in the region  $<600\text{nm}$  for samples of poor radiation resistance. This absorption causes the yellow to brown coloring shown in Fig. 17. It should be noted that the shape of the radiation induced absorption varies from crystal to crystal.

Radiation induced absorption results in significant degradation of the observed light yield. Samples showed saturation in their damage, which indicates the origin is most likely due to trace element impurities or defects in the crystal. The best samples show much less degradation in light attenuation length and light output.

### B. Radiation induced absorption

Fig. 19 shows the radiation induced absorption coefficient for crystal samples after a 30Gy dose of  $60\text{Co}$   $\gamma$  ray irradiation at at dose rate of 18Gy/min. Sample YY shows significant radiation induced absorption.

Sample J11 (significant scattering centers in bulk) was tested at the CUA, Caltech, IPN-Orsay, and Giessen facilities. The results agree within the uncertainty of the measurements. An illustration of the measurements at IPN-Orsay and Giessen is shown by the solid and dashed curves in Fig. 18.

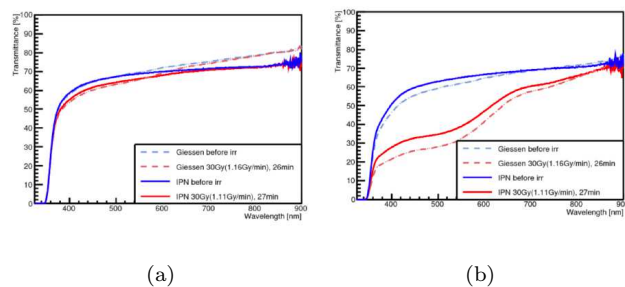


FIG. 18: (Color online) Transmittance ratio of after and before irradiation for a (a) good and (b) a bad crystal. The solid curves show measurements performed at IPN-Orsay and the dashed curves measurements performed at the Giessen facility.

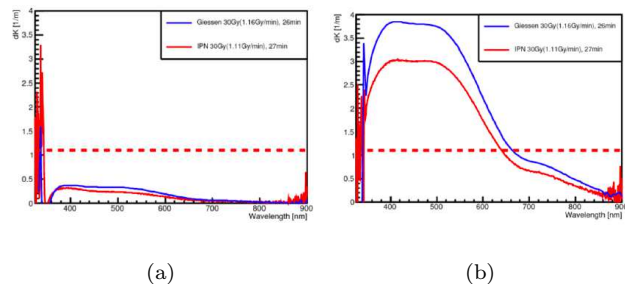


FIG. 19: (Color online) Absorption coefficient for a (a) good and (b) a bad crystal.

### C. Electron beam irradiation results

The transmittance of some of crystals changed more than 15% after an accumulated dose of 432 krad (at a dose rate of 1.3 Mrad/h), while others do not seem to show any effects of radiation damage. The change in transmittance for positions far from the front of crystals decreases with the distance. The effect of radiation damage is in part spontaneously recovered after a time period of 60 hours. Overall the results seem to suggest that the crystals can handle high doses at high dose rates.

One of the challenges in irradiation studies with beam is temperature control. Ideally one would control the temperature variation during the irradiation measurement within a few percent. This is difficult to achieve when working with an intense and narrowly focused beams, which give a high and concentrated dose to the crystals, and can even result in heating and thermal damage. As an example, for irradiation at a dose rate of 1.3 Mrad/hr, the temperature near the face of the crystal ramped up at a rate of  $0.5\text{ }^\circ\text{C}/\text{minute}$ . For irradiation at a dose rate of 2.6 Mrad/hr, a rise of the temperature of more than  $2\text{ }^\circ\text{C}/\text{minute}$  resulted in severe structural damage to the crystal after 10 minutes.

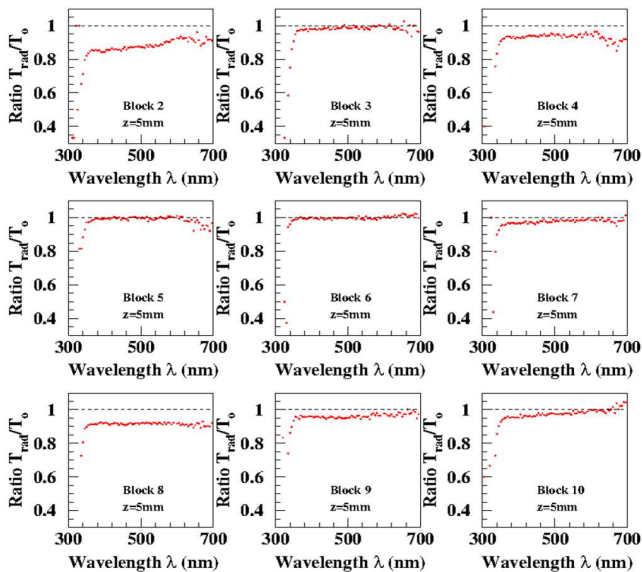


FIG. 20: (Color online) Transmission degradation of the  $\text{PbWO}_4$  blocks after 432 krad accumulated dose at dose rates of 1.3 Mrad/h. Ratio of transmissions after and before irradiation reflects the level of crystal degradation. For example, crystal J06 shown in the center panel was not damaged significantly.

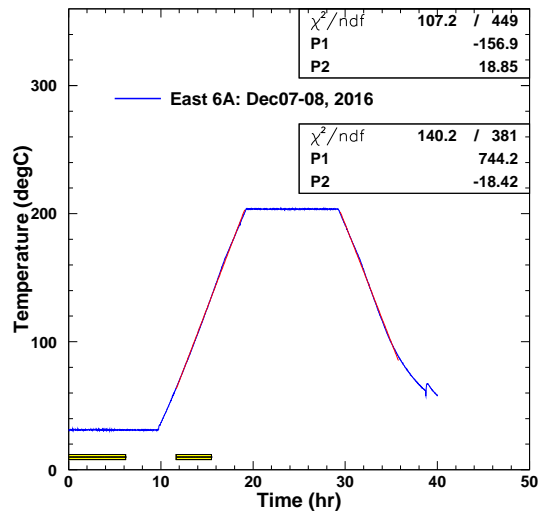


FIG. 21: (Color online) Temperature profile used for thermal annealing the crystals.

### 1. Thermal Annealing

Thermal annealing was done at 200°C for 10 hours. The protocol included a ramp up/down procedure at 18°C per hour starting/ending at room temperature. The temperature profile used to anneal the crystals is shown in Fig. 21. The transmittance of crystals exposed to an integrated dose of 30 Gy EM radiation is shown in Fig. 18. For crystals received from the vendors and not exposed to radiation no significant differences in optical properties were found before and after thermal annealing.

GRAPH OF IRRADIATED CRYSTAL BEFORE AND AFTER THERMAL ANNEALING

### 2. Optical Bleaching

Studies show that with blue (UV) light of wavelength  $\lambda \sim 400\text{-}700$  nm [24], nearly 90% of the original amplitude can be restored within 200 minutes with photon flux of  $\sim 10^{16}$  photon/s. Light of short wavelength is most effective for recovery, but recovery at longer wavelength (700-1000 nm) recovery is also possible. It works very well for low doses ( $\sim 3$  krad), but its efficiency compared to blue light is reduced by a factor of  $\sim 20\text{-}50$ . This can be compensated by using high intensity IR light ( $\geq 10^{16}$  photons/s per block). Studies show that at dose rates  $\sim 1$  krad/h with a IR light of  $\lambda \geq 900$  nm and intensity  $\sim 10^{16} - 10^{17}$   $\gamma/\text{sec}$  one may continuously recover degradation of the crystal [24? ]. Fig. ?? shows our results of the transmittance before irradiation(gray), after irradiation(dotted lines), and after 2 hours of curing with infrared(IR) and blue light with optical fibers.

## D. Thermal annealing and optical bleaching

The radiation induced absorption can be reduced by thermal annealing, in which color centers are eliminated by heating the crystal to a high temperature, or optical bleaching, in which light is injected into crystals. Color center annihilation is wave length dependent. Thermal annealing is beneficial to recover individual or small numbers of crystals. In a medium to large detector like the NPS optical bleaching is the preferred method.

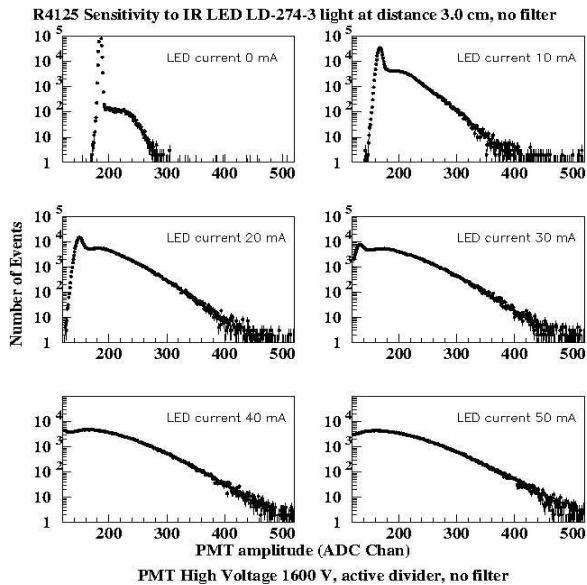


FIG. 22: Hamamatsu R4125 PMT sensitivity to IR light generated by LD-274-3 diode without filter.

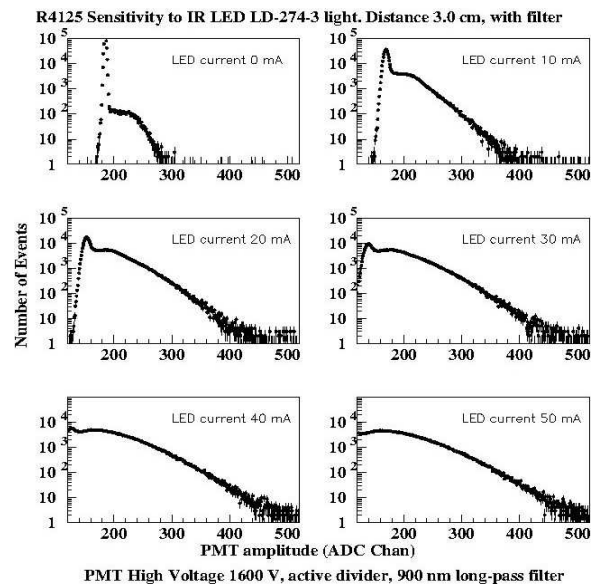


FIG. 23: Hamamatsu R4125 PMT sensitivity to IR light generated by LD-274-3 diode with  $\lambda > 900$  nm filter.

865 An advantage of IR curing is that it can in principle  
 866 be performed continuously, even without turning off the  
 867 high voltage on the PMTs as long as the IR light is  
 868 out of the PMTs quantum efficiency region. To test  
 869 this assumption the emission intensity of the Infrared  
 870 LED LD-274-3 and TSAL7400 versus driving current  
 871 have been measured. The peak wavelengths are 950 nm  
 872 for LD-274-3, and 940 nm for TSAL7400.

873 The LEDs were mounted on a special support struc-  
 874 ture and the intensity of the emitted light was measured  
 875 with a calibrated photodiode (S2281) with an effective  
 876 area of 100 mm<sup>2</sup>. The distance between LED and photo-  
 877 diode was variable from 0.5 cm to 20 cm. All equipment  
 878 was installed in a dark-room. The photodiode dark cur-  
 879 rent when the LED was off was on the level of  $\sim 0.001$   
 880 nA.

881 To determine the quantum sensitivity to IR light,  
 882 a phototube (Hamamatsu R4125) was installed at the  
 883 front of the LED. The measurements were done at dif-  
 884 ferent LED driving currents (from 0 up to 100 mA), at  
 885 distances 0.5 cm, 3cm, and 16 cm (18 cm), with and  
 886 without a PbWO<sub>4</sub> crystal at the front of the PMT. To  
 887 eliminate contamination of short wavelength light in the  
 888 emission spectrum of the IR LEDs we made measure-  
 889 ments with and without 900 nm long-pass filter. The  
 890 PMT amplitude spectra for LD-274-3 measured at a dis-  
 891 tance of 3 cm and driving currents of 0-50 mA are shown  
 892 in Fig. 22 and Fig. 23. The results show that the PMT  
 893 R4125 has a very low, but not negligible, efficiency rela-  
 894 tive to infrared light. Since even a low quantum effi-  
 895 ciency may reduce the PMT live time for an IR curing  
 896 flux of photons of  $N \sim 10^{16} - 10^{17}$   $\gamma/sec$  and because of  
 897 the lower efficiency relative to blue light the NPS optical  
 898 bleaching system will be based on blue (UV) light.

## 909 VII. STRUCTURAL AND CHEMICAL 900 ANALYSIS

901 The chemical composition of the crystals were investi-  
 902 gated at the Vitreous State Laboratory (VSL) using  
 903 a combination of standard chemical analysis methods  
 904 including XRay Fluorescence (XRF) and ICP-MS. The  
 905 surface analysis was performed with a scanning electron  
 906 microscope with EDS and WDS systems and nanoma-  
 907 nipulator (JEOL 6300, JEOL 5910).

### 908 A. Surface Properties

909 Figure 24 shows the surface quality of representative  
 910 crystals from Crytur at 50  $\mu m$  and SICCAS at 500  $\mu m$ .  
 911 For comparison, a BTCP sample was analyzed as well.  
 912 The surface of the Crytur crystal is well-polished with  
 913 negligible mechanical flaws. The SICCAS crystal has  
 914 long scratches on the surface and also other flaws as  
 915 shown. The BTCP crystal surface has scratches, which  
 916 is expected as this crystal had been shipped multiple  
 917 times without re-polishing.

918 Looking even deeper into the crystal defects of the  
 919 SICCAS samples (see Fig. 25) reveals bubbles and deep  
 920 pits up to 20  $\mu m$  inside the bulk. The size of these  
 921 bubbles can be on the order of 100  $\mu m$ . These flaws can  
 922 be correlated with an observed very high, but position  
 923 dependent light yield inducing non-uniformities, as well  
 924 as a very low transmittance around XXX nm.

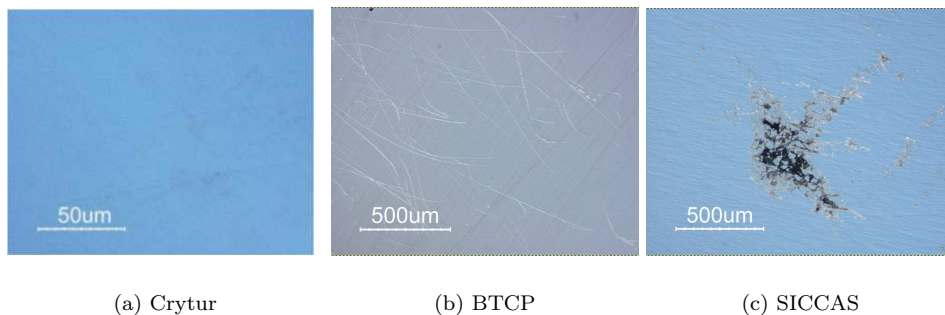


FIG. 24: (Color online) Microscope surface analysis of PbWO<sub>4</sub> crystals from Crytur (top left, a), BTCP (top right, b) and SICCAS produced in 2017 (bottom, c).

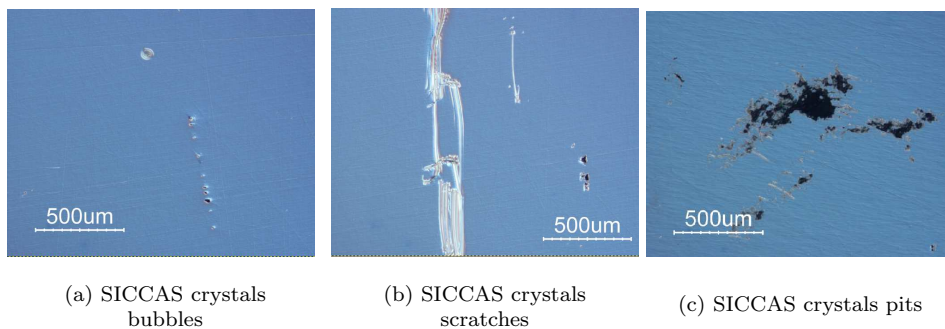


FIG. 25: (Color online) Microscope images of bubbles (a), deep scratches (b) and pits (c) observed in SICCAS crystals produced in 2017.

## B. Chemical composition analysis

Real crystals contain large numbers of defects, ranging from variable amounts of impurities to missing or misplaced atoms or ions. It is impossible to obtain any substance in 100% pure form. Some impurities are always present. Even if a substance were 100% pure, forming a perfect crystal would require cooling infinitely slowly to allow all atoms, ions, or molecules to find their proper positions. Cooling usually results defects in crystals. In addition, applying an external stress to a crystal (cutting, polishing) may cause imperfect alignment some regions of with respect to the rest, In this section, we discuss how chemical composition can impact some of the crystal properties.

Samples on the order of 100 microgram were taken from each crystal using a method developed by the VSL. The method is non-destructive and does not impact the crystal optical properties. The latter was verified with dedicated measurements. Approximately 10-15% of the crystals, which were also characterized for optical properties, were investigated in this study.

Figure 26 shows a general overview of the variation in composition for a representative set of SICCAS crystals in terms of the element oxides. "Good" crystals are denoted as those that pass all optical specifications, while

"bad" crystals fail all or a large fraction thereof. The two major materials (PbO and WO<sub>3</sub>) used in crystal growing are not shown. The variation in these materials among all good and bad crystals is small (0.5-0.7% on average), which one might interpret as differences in optical properties being due to other contributions in the chemical composition (see results of statistical analyses in the next paragraphs) or mechanical features. The results in Figure reffig:SICCAS-crystals-composition suggest that good crystals have a noticeable contribution from iron oxide (green column) and smaller contributions from at most two others. On the other hand, bad crystals have at least three contributions other than iron.

To investigate the importance of the variation in lead and tungsten oxides, as well as those of the other elements observed in chemical composition analysis, statistical analyses were carried out. The first method is a multivariate approach in which correlations are estimated by a pairwise method. The results are shown in Table IV. A clear dependence of the optical transmittance on the stoichiometry of lead and tungsten oxides can be seen. The light yield does not seem to depend on this stoichiometry.

The second statistical method uses partial least squares to construct two correlation models and assess effects of individual variables. The results for two result-



	Al2O3	CaO	Cl	Cr2O3	CuO	Fe2O3	NiO	PbO	Rb2O	SiO2	WO3	ZnO	ZrO2	LY	LT420
Al2O3	1.0000	-0.0637	0.0500	0.0222	-0.5035	0.6193	-0.1994	0.2246	0.1136	-0.4142	-0.3617	0.2726	0.2487	0.2094	-0.1775
CaO	-0.0637	1.0000	-0.1947	-0.0910	-0.0910	-0.2581	-0.3309	-0.0255	-0.0910	-0.1440	0.2046	-0.1271	-0.2315	-0.3779	-0.1202
Cl	0.0500	-0.1947	1.0000	-0.1337	0.2209	0.4481	0.6386	0.0721	-0.1337	-0.0945	-0.3613	-0.1868	0.0636	-0.2777	-0.1756
Cr2O3	0.0222	-0.0910	-0.1337	1.0000	-0.0625	0.0620	0.3061	0.3970	-0.0625	-0.2357	-0.3078	-0.0873	-0.1590	-0.2804	-0.4934
CuO	-0.5035	-0.0910	0.2209	-0.0625	1.0000	-0.1440	0.2086	0.2237	-0.0625	0.0827	-0.1630	-0.0873	-0.1590	-0.0919	-0.1861
Fe2O3	0.6193	-0.2581	0.4481	0.0620	-0.1440	1.0000	0.1952	0.4125	-0.2305	-0.4911	-0.7115	0.3980	0.4512	-0.1540	-0.2958
NiO	-0.1994	-0.3309	0.6386	0.3061	0.2086	0.1951	1.0000	0.1436	-0.2273	-0.0730	-0.2637	-0.1491	-0.3345	-0.3974	-0.1615
PbO	0.2246	-0.0255	0.0721	0.3970	0.2237	0.4125	0.1406	1.0000	-0.0700	-0.4356	-0.8960	0.3456	-0.0146	-0.1618	-0.7324
Rb2O	0.1136	-0.0910	-0.1337	-0.0625	-0.0625	-0.2305	-0.2273	-0.0700	1.0000	-0.2357	0.2155	-0.0873	-0.1590	0.0512	0.0207
SiO2	-0.4142	-0.1440	-0.0945	-0.2357	0.0827	-0.4911	-0.0730	-0.4356	-0.2357	1.0000	0.3862	-0.0763	-0.1999	0.2082	0.6228
WO3	-0.3617	0.2046	-0.3613	-0.3078	-0.1630	-0.7115	-0.2637	-0.8960	0.2155	0.3862	1.0000	-0.4071	-0.2302	0.1556	0.6197
ZnO	0.2726	-0.1271	-0.1868	-0.0873	-0.873	0.3980	-0.1491	0.3456	-0.0873	-0.0763	-0.4071	1.0000	0.1292	-0.2337	0.0767
ZrO2	0.2487	-0.2315	0.0636	-0.1590	0.1590	0.4512	-0.3345	-0.0146	-0.1590	-0.1999	-0.2302	0.1292	1.0000	0.4764	-0.0142
LY	0.2094	-0.3779	-0.2777	-0.2804	-0.0919	-0.1540	-0.3974	-0.1618	0.0512	0.2082	0.1556	-0.2337	0.4764	1.0000	0.1931
LT420	-0.1775	-0.1202	-0.1756	-0.4934	-0.1861	-0.2958	-0.1615	-0.7324	0.0207	0.6228	0.6197	0.0767	-0.0142	0.1931	1.0000

TABLE IV: Multivariate analysis results. A clear dependence of optical transmittance on PbO/WO<sub>3</sub> stoichiometry can be observed. Light yield appears independent on it.

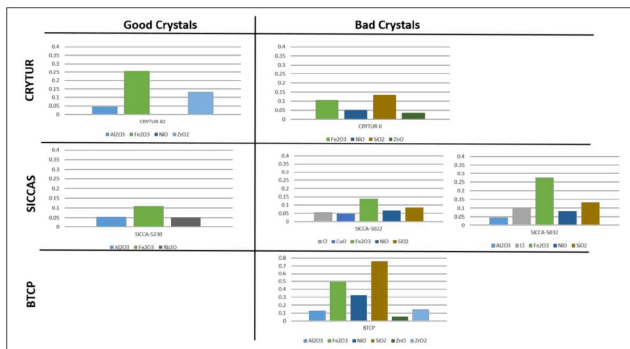
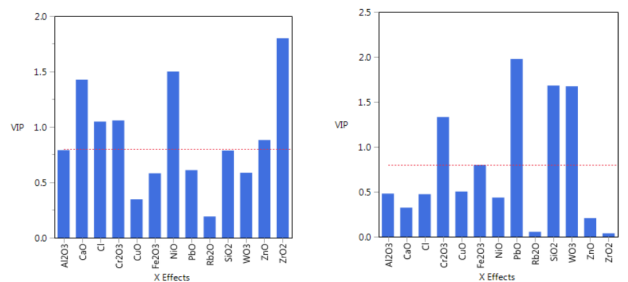


FIG. 26: (Color online) Crystal composition from XRF analysis. The two major materials (PbO and WO<sub>3</sub>) used in PbWO<sub>4</sub> crystal growth are not shown.



(a) Light yield vs composition

(b) Transmittance vs composition

FIG. 27: (Color online) Effect of individual elements of chemical composition on light yield (a) and optical transmittance (b) based on a partial least square statistical analysis.

976 ing models assessing the impact of chemical composition  
 977 on light yield and optical transmittance is shown in Fig-  
 978 ure 27. Zr, Ni, and Ca seem to be most relevant for  
 979 light yield, while Si and to a lesser extent Cr seem most  
 980 relevant for transmittance at 420 nm.

## 981 VIII. BEAM TEST PROGRAM WITH 982 PROTOTYPE

983 A first prototype was constructed at JLab using 3D  
 984 printing technology. Fig. 28 shows a schematic view of  
 985 the prototype mechanical structure. The prototype consists  
 986 of a 3x3 matrix of PWO crystals, placed inside a  
 987 brass box. The stack of crystals is fixed to the box using  
 988 3D-printed plastic holders. The front face of the proto-  
 989 type box is covered with a 2 mm thick plastic plate. The  
 990 plastic mesh plate is placed in front of the crystal stack  
 991 and is mounted to the prototype frame to prevent indi-  
 992 vidual crystals from sliding in the forward direction. The  
 993 crystals are wrapped with an 65 m ESR reflector and a  
 994 30 m thick Tedlar film to provide light tightness. Each

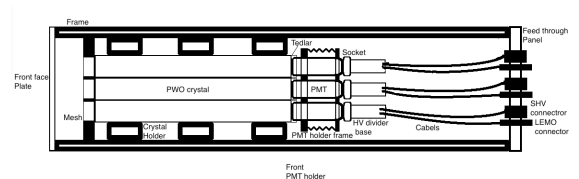


FIG. 28: (Color online) Neutral Particle Spectrometer (NPS) prototype schematic view.

crystal is coupled to a R4125-01 Hamamatsu PMT using  
 an optical grease. The PMTs are attached to the crystals  
 using two plastic holder plates. The front plate is  
 attached to the side wall of the prototype frame and has  
 nine holes allowing the PMT's to slide in the forward  
 direction towards crystals. The movable back PMT  
 plate holds the PMTs and provides pressure needed for  
 optical coupling using springs, which are connected between  
 the

plates in each corner. The back plate has holes for PMT pins, to attach dividers. The PMT is powered and read out using a HV divider with an integrated preamplifier designed at Jefferson Lab. High voltage and signal cables are connected to the SHV and LEMO connectors installed in the back plate of the prototype box.

Performance of the calorimeter prototype was studied using secondary electrons provided by the Hall D Pair Spectrometer (PS)[28]. The schematic view of the Pair Spectrometer is presented in Fig. 29 Electron-positron pairs are created by beam photons in a 750 m Beryllium converter. The produced leptons are deflected in a 1.5 T dipole magnet and are detected using two layers of scintillator counters positioned symmetrically with respect to the photon beam line. In each arm, there are 8 coarse counters and 145 high-granularity counters. The coarse counters are used in the trigger. The high-granularity hodoscope is used to measure the lepton momentum; the position of each counter corresponds to the specific energy of the deflected lepton. Each detector arm covers a momentum range of  $e^-$  between 3.0 GeV/c and 6.2 GeV/c. The energy resolution of the pair spectrometer is estimated to be better than 0.6%. The calorimeter prototype was positioned behind the PS as shown in Fig. 29 The energy of electrons passing through the center of the middle module was measured using the PS hodoscope and corresponded to 4.7 GeV. High voltages for nine prototype channels were provided by CAEN A1535SN module. Signals from PMTs are digitized using a twelve-bit 16 channel flash ADC operated at 250 MHz sampling rate [29]. Digitized amplitudes are integrated in a time window of 68 ns. Readout of the prototype was integrated to the global GlueX DAQ system. Data were collected in parallel with the GlueX [30] using the pair spectrometer trigger, which was produced by the electron-positron pair and is required for the luminosity determination in GlueX.

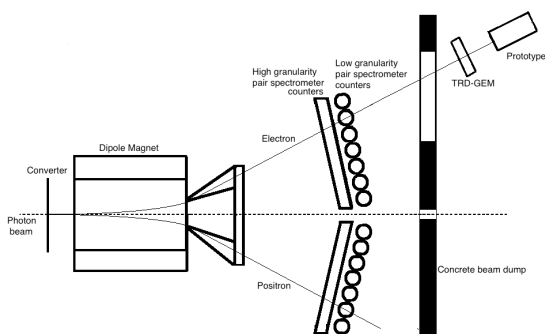


FIG. 29: (Color online) Position of the calorimeter behind the HallD Pair Spectrometer.

We calibrated the energy response (gain factors) of each calorimeter module using two independent methods:

- Direct energy calibration. Three modules in each

row were calibrated by measuring energy depositions (in units of fadc counts) for electrons incident on the middle of each cell. Modules from other rows were subsequently calibrated by lowering and lifting the prototype by 2 cm (the module size) and exposing corresponding rows to the beam.

- Using regression calibration. Calibration coefficients were obtained by minimizing the difference between the total energy deposited in the 3x3 calorimeter prototype and the electron energy reconstructed by the Pair Spectrometer. The calibration was performed for events where electrons hit the center of the middle module:

$$\sum_{events} \left( \sum_{i=1}^{Nseg} k_i A_i - E_{ps} \right)^2 \rightarrow min \quad (6)$$

where Nseg is the number of modules in the cluster,  $k$  is the calibration coefficient,  $A$  is the signal pulse integral, and  $E_{ps}$  is the electron energy measured by the pair spectrometer.

These two calibration methods provided consistent results. Fig. 30 a) and b) show reconstructed energy in the 3x3 calorimeter for 4.7 GeV electrons incident on the middle of the central module. The calorimeter was constructed using CRYTUR and SICCAS crystals and was tested during the spring run of 2019. The measured resolution was 1.6% and 1.5% for CRYTUR, SICCAS crystals, respectively. We also observed about 6% larger light yield for SICCAS crystals, which can potentially account for slightly better energy resolution (Note: SICCAS crystals are known to have slightly larger light yield, though are less radiation resistant compared with CRYTUR crystals).

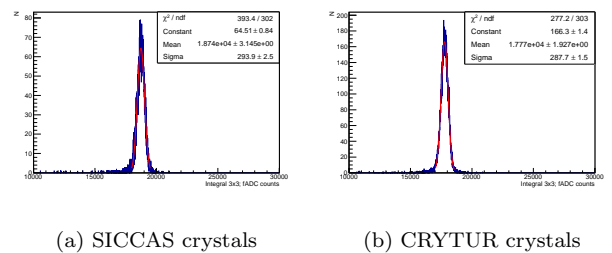


FIG. 30: (Color online) Total energy reconstructed in the 3x3 calorimeter for 4.7 GeV electrons

## IX. GLASS SCINTILLATORS AS ALTERNATIVE TO CRYSTALS

Glasses are much simpler and less expensive to produce than crystals and thus offer great potential if competitive performance parameters can be achieved. Early

tests have shown good quality and radiation hardness. Due to the different properties, glass would require a 40 cm longitudinal dimension, but could be made to size for different detector regions.

In the past, production of glass ceramics has been limited to small samples due to difficulties with scale-up while maintaining the needed quality. Some of the most promising materials include cerium doped hafnate glasses and doped and undoped silicate glasses and nanocomposites. All of these have major shortcomings including lack of uniformity and macro defects, as well as limitations in sensitivity to electromagnetic probes. One of the most promising recent efforts is DSB:Ce, a cerium-doped barium silicate glass nanocomposite. Small samples of this material exhibit up to one hundred times the light yield compared to  $\text{PbWO}_4$  and are in many respects competitive with  $\text{PbWO}_4$ . However, the issues of macro defects, which can become increasingly acute on scale-up, and radiation length still remains to be addressed.

## X. SUMMARY

High resolution electromagnetic calorimeters are an essential piece of equipment at upcoming NPS experiments at 12 GeV Jefferson Lab and the Electron-Ion Collider. This instrument enables precise measurements of DVCS, the method of choice in the program of the three-dimensional imaging of nucleon and nuclei and unveiling the role of orbital angular motion of sea quarks and gluons in forming the nucleon spin. To satisfy the experimental requirements the EMCAL should provide: 1) good resolution in angle to at least 1 degree to distinguish between clusters, 2) energy resolution to a few  $\%/\sqrt{E}$  for measurements of the cluster energy, and 3) the ability to withstand radiation down to at least 1 de-

gree with respect to the beam line. A solution based on  $\text{PbWO}_4$  would provide the optimal combination of resolution and shower width at small angles where the tracking resolution is poor.

Since the construction of the CMS ECAL and the early construction of the PANDA ECAL the global availability of high quality  $\text{PbWO}_4$  crystals has changed dramatically. In this paper we have analyzed samples from SICCAS and samples from CRYTUR, the only two vendors worldwide with mass production capability. Samples were produced between 2014 and 2019. Based on NPS specifications, the overall quality of CRYTUR crystals was found to be better than that of SICCAS samples. Categories in which CRYTUR samples performed better include uniformity of samples, e.g. in transmittance and light yield, and considerably better radiation hardness. CRYTUR samples also showed fewer mechanical defects, both macroscopic and microscopic.

## ACKNOWLEDGMENTS

This work is supported in part by NSF grants PHY-1530874, PHY-1306227, PHY-1714133, and the Vitreous State Laboratory (VSL). The detector benefited greatly from components graciously provided by both the PANDA collaboration and Jefferson Lab Hall A/C (crystals and PMTs). We explicitly are grateful to Rainer Novotny and Valera Dormenev from Giessen U. for support with constructing our crystal test setups and providing their facilities for selected optical and irradiation tests. We would also like to thank Ren-Yuan Zhu from Caltech for tests of selected samples, Craig Woody from Brookhaven National Lab, and Carl Zorn from the Detector Group of the Jefferson Lab Physics Division, for help during various stages of the work. The Southeastern Universities Research Association operates the Thomas Jefferson National Accelerator Facility under the U.S. Department of Energy contract DEAC05-84ER40150.

- 
- [1] JLab experiment E12-13-007: Measurement of Semi-Inclusive  $\pi^0$  Production as Validation of Factorization, R. Ent, T. Horn, E. Kinney, H. Mkrtchyan, V. Tadevosyan spokespersons. PAC40 approved, 25 days, A-rating.
- [2] JLab experiment E12-13-010: Exclusive Deeply Virtual Compton and Neutral Pion Cross-Section Measurements in Hall C. C. Muoz Camacho, R. Paremuzyan, T. Horn, J. Roche spokespersons, PAC40 approved, 53 days, A rating.
- [3] JLab experiment E12-14-003: Wide-angle Compton scattering at 8 and 10 GeV photon energies. D.J. Hamilton, S. irca, B. Wojtsekhowski spokespersons. PAC45, approved, 42 days, A- rating.
- [4] JLab experiment E12-14-005: Wide angle Exclusive Photoproduction of  $\pi^0$  Mesons. D. Dutta, M. Amaryan, H. Hao, M. Kunkel, S. Sirica, I. Strakovski spokespersons, PAC45 approved, 42 days, B rating.
- [5] X. -D. Ji, Deeply-Virtual Compton Scattering, Phys. Rev. D 55, 7114 (1997), arXiv:hep-ph/9609381
- [6] A. Accardi et al., Electron-Ion Collider: The Next QCD Frontier understanding the glue that binds us all, Eur. Phys. J. A52 (2016) no.9, 268; arXiv.1212.1701, BNL-98815-2012, JLAB-PHY-12-1652 (2012)
- [7] Electron-Ion Collider Detector Requirements and R&D Handbook v1.1 (2019). Available: [http://www.eicug.org/web/sites/default/files/EIC\\_HANDBOOK\\_Electron-Ion\\_Collider\\_Documentation\\_Series\\_\(2019\).Available:https://www.eiccenter.org/physicists](http://www.eicug.org/web/sites/default/files/EIC_HANDBOOK_Electron-Ion_Collider_Documentation_Series_(2019).Available:https://www.eiccenter.org/physicists)
- [8] M. Kubantsev, I. Larin, A. Gasparyan, Performance of the PrimEx Electromagnetic Calorimeter, AIP Conf. Proc. 867:51-58, 2006; DOI: 10.1063/1.2396938
- [9] A.N. Belsky et al., Chem. Phys. Lett. 243 (1995), 552
- [10] R.Y. Zhu et al., CMS TN/95-157
- [11] V.A. Batarin et al., Nucl. Phys. B150 (2006), 262
- [12] A. Fyodorov et al., Rad. Meas. 26 (1996), 107
- [13] P. Achenbach et al., Nucl. Instrum. Meth. A290 (1990), 385

- 1180 [14] V. Dormenev et al., Comparison of Radiation Damage 1201  
 1181 Effects in PWO Crystals under 150 MeV and 24 GeV 1202  
 1182 High Fluence Proton Irradiation, IEEE Trans. on Nucl. 1203  
 1183 Sci. Vol 61, No. 1, 2014, 501-506 1204
- 1184 [15] L. Nagornaya et al., IEEE Trans. on Nucl. Science 44 1205  
 1185 (1997) 866 1206
- 1186 [16] R.Y. Zhu et al., IEEE Trans. on Nucl. Science 45 (1998) 1207  
 1187 686 1208
- 1188 [17] P. Leqcoq et al., Nucl. Instrum. Meth. A365 (1994), 291 1209
- 1189 [18] S. Chao-Shu, Chin. Phys. Lett. 15 (1998), 55 1210
- 1190 [19] N.R. Krutyak et al., J. Appl. Spectr. 79 (2012), 211 1211
- 1191 [20] Semenov et al. NIMA 582 (2007) 575-580 1212
- 1192 [21] R. Mao et al., IEEE Trans. Nucl. Sci., Vol. 51, No. 4, 1213  
 1193 (2004) 1777. 1214
- 1194 [22] M.V. Korzhik et al, Nucl. Inst. Methods A 365 (1995) 1215  
 1195 291; LAPP-EXP 94-01 (1994) 1216
- 1196 [23] R.Y. Zhu, IEEE Trans. Nucl. Sci. NS-51 1777 1217
- 1197 [24] R. W. Novotny, J. Phys. Conf. Ser. 404, 2012, p.012063). 1218
- 1198 [25] R. W. Novotny, IEEE-2009-05402124. 1219
- 1199 [26] R.Y. Zhu et al., Nucl. Instrum. Method. A 376 (1996) 1220  
 1200 319-334.
- [27] S. Baccaro et al., Nucl. Instrum. Method. A 385 (1997)  
 209-214.
- [28] F.Barbosa, C.Hutton, A.Sitnikov, A.Somov, S.Somov,  
 I.Tolstukhin, Pair Spectrometer hodoscope for HallD  
 at Jefferson Lab, Nucl.Instrum. & Meth.A795,376-  
 380(2015).
- [29] F. Barbosa et. al., Proceedings of IEEE nuclear Sympo-  
 sium, Hawaii,USA (2007).
- [30] Jlab Experiment E12-06-12, (2006)  
<http://www.jlab.org/exp.prog/proposals/06/PR12-06-102.pdf> .  
 scintillation crystals for the CMS Electromagnetic  
 Calorimeter. Published by JINST, 25 March 2010,  
 JINST 5 P03010.  
 radiation hardness of PWO scintillators to be used at  
 CMS electromagnetic calorimeter at CERN. Proc. Int.  
 Conference in Inorganic Scintillators and their Applica-  
 tions, SCINT95. P. Dorenbos and C.W.E. van Eijk eds.  
 Delf, The Netherlands, August 28 - September 1 (1995),  
 pg 282-285 [ISBN 90-407-1215-8].